Characterisation of Acoustic Emission Sources in a Rock Salt Specimen under Triaxial Load

Gerd Manthei
Gesellschaft für Materialprüfung und Geophysik
Dieselstraße 6a, D-61239 Ober-Mörlen, Germany
Phone.- +49-6002-7971, Fax.- +49-6002-7973, E-Mail.- gmugmbh@t-online.de

ABSTRACT

This study presents the application of an automated moment tensor analysis procedure on microcracks which were generated during a triaxial compression test of a cylindrical rock salt specimen (diameter 150 mm, length 300 mm). The acoustic emission signals were detected in a frequency range between 20 kHz and 1 MHz using 12 acoustic emission sensors mounted on the surface of the specimen cylinder.

The moment tensor analysis was applied to about 30,000 events, which were precisely located using at least 16 P- and S-wave arrival times. For more than 40 per cent of these events, i.e. approximately 12,500 events, stable moment tensor solutions could be evaluated using the first motion of the P-wave radiation patterns. Most of the evaluated events showed significant isotropic source components which is in good agreement with dilatation of rock during compressional loading. The majority of the events were caused by tensile opening which is leading to dilatation of the rock. The tension (T) axes which are normal to the crack plane of these tensile microcracks, were predominantly orientated in radial direction of the cylindrical specimen, perpendicular to the maximum principal stress, which is in axial direction. The direction of the tensile opening calculated by the moment tensor evaluation coincides very well with the direction of the minimum principal stress.

The applied collapsing method discovers cellular structures with a cell size in the range of a few centimetres. However, it seems that the events occur only in zones where the cell interfaces are favourably orientated in the stress field. These events are attributed to cracking at grain interfaces which occurs in rock salt under very slow creep loading above the dilatancy boundary.

1 INTRODUCTION

The scope of this work is to determine mechanisms of acoustic emission (AE) events which were recorded during a compression test of a rock salt specimen under confining pressure. In analogy to earthquakes, AE sources (like microcracks) radiate elastic energy and, consequently, it is possible to investigate them by similar techniques as used in seismology. With other words, the mechanisms of earthquakes and AE sources are in principal the same, in spite of the fact that strengths and frequencies differ by orders of magnitude (Eisenblätter 1980). Therefore, it is possible to apply the moment tensor method which describes mechanisms of general seismic sources, to these events whose frequencies range between 20 kHz and 1 MHz. The moment tensor method was introduced into seismology by Gilbert (1970). A review about several applications of AE measurements in rock mechanics studies is given in Manthei et al., 2000.

In principle, two methods are in common use in source mechanism studies. In earthquake seismology, the classical method is the fault-plane solution method. This method uses polarities and ray directions of the P-wave to constrain possible double-couple (DC) fault-plane solutions and requires a very good sensor coverage of the focal sphere. The fault-plane solution method assumes pure shear slip along the fault plane which is realistic for tectonic earth-

quakes. Therefore, the fault-plane solution method is especially adapted to the situation of tectonic earthquakes within the earth where volume changes normally cannot occur. On the contrary, in the case of laboratory investigations on rock specimens under uniaxial or triaxial compressional load, volume changes in the source play an important role. This fact was confirmed in many laboratory experiments on rock samples under compressional stress conditions. The experiments figured out that microcracking leads to a non-reversible increase of the rock volume which is called dilatancy (Brace et al. 1966, Scholz 1968a, Lockner et al. 1977, Hunsche et al. 1999, Alkan et al. 2002). Dilatancy can be explained as volume expansion which is caused by tensile opening.

In contrast to the fault-plane solution method, the more complex moment tensor method is capable to describe sources with isotropic components like tensile cracks as well as deviatoric sources like shear cracks or a mixture of both source types. The isotropic source components can be easily obtained using the isotropic part defined as one-third of the trace of the moment tensor. With the moment tensor method the source mechanisms are estimated in a least-square inversion calculation from amplitudes of the first motion as well as from full waveforms of compressional (P) and shear (S) waves which requires additional knowledge about the transfer function of the medium (the so called Green's function) and sensor response. In this paper we would like to demonstrate the application of the moment tensor method to analyse automatically thousands of AE events. The automatic procedure is separated into source location, data extraction, and stability check of the inversion calculation.

2 THEORY

In the following, a short description of the theory of moment tensor representation for point sources in homogeneous media will be given. A detailed description of the theory and general properties of moment tensor is given in the textbook of Aki & Richards (2002) and in the student's guides of Pujol & Hermann (1990) or Jost & Hermann (1989).

The n-component of observed displacement at an observation point specified by coordinates $\vec{x}$ and time t is given with the moment tensor representation of a seismic point source as:

$$u_n(\vec{x},t) = \int_{-\infty}^{+\infty} M_{pq}(\tau)\,\frac{\partial}{\partial \xi_q}\,G_{nq}(\vec{x};t-\tau;\vec{\xi},0)\,d\tau. \qquad (1)$$

In this formula u_n is the displacement ($n = 1...3$), M_{pq} the seismic moment tensor, G_{np} the Green's function tensor, $\vec{x}$ and $\vec{\xi}$ are space coordinates. Equation (1) can be used to describe the excitation of a source in a material where the forces and its moments in the source region must be self-equilibrating. In the case in which each of the components M_{pq}. shares the same source-time function $S(t)$, Equation (1) becomes in the far field

$$u_n(\vec{x},t) = \left[M_{pq} \cdot \dot{S}(t) \right] * G_{np,q}. \qquad (2)$$

The asterisk denotes the convolution in the time domain and $\dot{S}(t)$ is the time derivative of the source time function. In the ray-theoretical limit, the Green's function tensor in source Equation (2) can be further simplified. For this purpose, we introduce a local coordinate system with origin at the source location. The azimuth angle φ (angle in horizontal plane) is measured clockwise from north and θ is the angle between the normal vector of the horizontal plane and radius vector between source and sensor positions (Aki & Richards, 2002). The n-component of displacement of the P-wave is:

$$u_n^P = I_n \sum_{k=1}^{6} m_k \cdot a_{nk}, \qquad (3)$$

with

$$a_{n1} = \sin^2 \vartheta \cdot \cos^2 \varphi, \quad a_{n2} = \sin^2 \vartheta \cdot \cos 2\varphi, \quad a_{n3} = \sin^2 \vartheta \cdot \sin^2 \varphi,$$
$$a_{n4} = \sin 2\vartheta \cdot \cos \varphi, \quad a_{n5} = \sin 2\vartheta \cdot \sin \varphi, \quad a_{n6} = -\sin^2 \vartheta + 1$$

and

$$m_1 = M_{11}, \quad m_2 = M_{12}, \quad m_3 = M_{22}, \quad m_4 = M_{13}, \quad m_5 = M_{23}, \quad m_6 = M_{33}.$$

3 EXPERIMENTAL SET-UP AND PERFORMANCE OF THE EXPERIMENT

The experiment on the cylindrical salt rock specimen (diameter 150 mm, length 300 mm) from the salt mine Asse in Germany was carried out in the laboratory of the Department for Waste Disposal Technology and Geomechanics at the Technical University of Clausthal, Germany. A triaxial hydraulic loading system was used for the test, which contains the hydraulic cell where cylindrical rock samples covered by a viton sleeve are subjected to high hydraulic pressure up to 75 MPa and additional axial force up to 2,500 kN (Lux, et al. 2000). During the test the axial displacement and axial force, the radial pressure, and the volume change (dilatancy) of the specimen could be measured and displayed on-line on the screen of the computer. The digitized data were stored every five seconds on the hard disk. The pore volume of the specimen corresponds to the change of oil volume in the triaxial cell, which was measured using a double acting measuring hydraulic cylinder. The accuracy of the dilatancy measurement is about 0.0025 per cent of the total volume within the load cell. At the beginning of the test the specimen was compacted for 16 hours over night under isotropic stress conditions at a pressure of 20 MPa in order to close open fractures at the surface of the specimen, which were eventually caused by manufacturing of the sample. After the compaction phase the test was performed applying a constant axial displacement rate of 0.15 mm per minute and a radial pressure of 5 MPa.

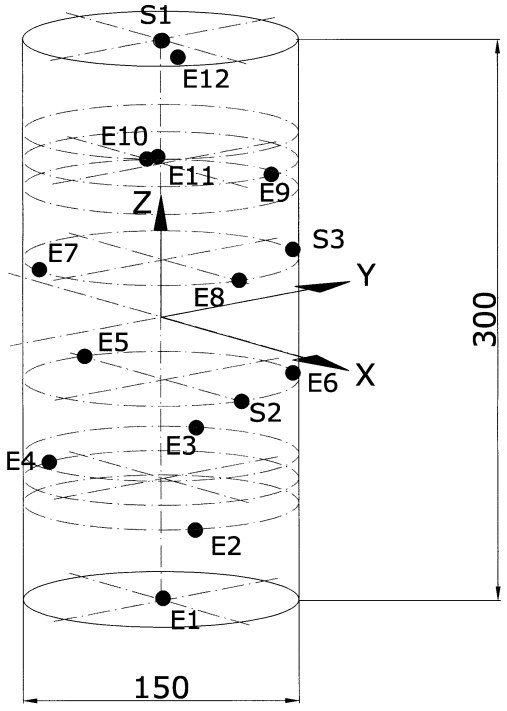

Figure 1: *Geometry of the rock salt specimen and location of AE sensors positions*

The AE sensor arrangement is shown in **Figure 1**. A stiff strain gauge glue was used to fix the sensors to the surface of the boreholes. The AE measuring system includes three four-channel transient recorder cards in a personal computer. The transient recorder cards (sampling rate 10 MHz, resolution 14 bit, storage capacity 512 kByte per channel) were read each time when at least two channels were hit. The digitized signals were stored on the hard disk of the personal computer. The overall duration of the test was about 4.3 hours.

4 SOURCE LOCATION

During the experiment about 64,000 events were recorded by more than five channels, 90 per cent of these were locatable. At about 21 mm axial compression most of the sensors were

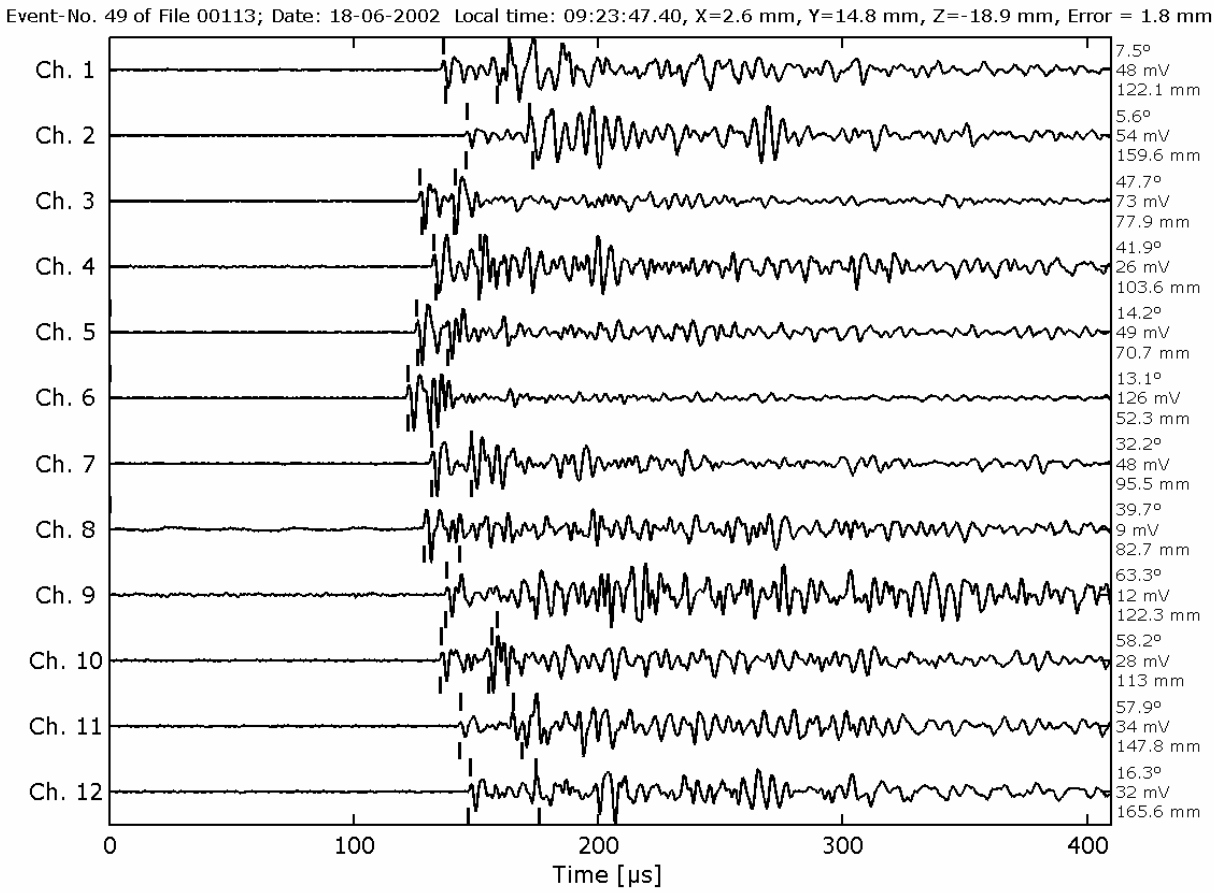

Figure 2: *Event originating from the lower half of the specimen. The onsets of the picked and calculated first (P-wave) and second (S-wave) arrivals are marked by ticks above and below the signal trace, respectively.*

damaged or the measuring cables were ruptured due to the high deformation. Therefore, after this point a three-dimensional location was no longer possible.

The location of the events was made off-line after the test. As the signals showed a surprisingly good signal-to-noise ratio **(Figure 2),** automatic location was possible. The location procedure starts with lowpass filtering of the signals at a corner frequency of 500 kHz. After filtering, all signals showing a signal-to-noise ratio greater than 5 were taken into consideration for source location. In a first step events with at least five P-wave arrival times detected at a very low amplitude threshold of 2.5 per cent of the peak amplitude were located. The location was considered valid if the location error was smaller than 5 mm. Otherwise the location was repeated twice. In the first variant the first hit channel was ignored and in the second variant the channel with the greatest P-wave travel time residuum was ignored. The variant with smaller location error was kept. This procedure was repeated as long as the location error was smaller than 5 mm or less than five P-wave onsets were left for location. In the latter case the event was rejected.

After source location using only P-wave arrival times, in a second step the location procedure was repeated using P- and S-wave arrivals. To this end, the onsets of the S wave were sought around the calculated P-wave arrival times. The trigger threshold for the S wave was chosen in the interval between noise level after the calculated P-wave arrival and peak amplitude of the signals. The applied S-wave trigger threshold at 35 per cent of the said interval is much higher than the P-wave threshold. Similar to the previous location using only P-wave onsets, the channel with the greatest S-wave travel time residuum was ignored. An event was

rejected when the location error was greater than 5 mm or less than eight P- and S-wave onsets had remained for location.

Figure 2 shows the automatically detected P-wave arrivals and S-wave arrivals which are marked by ticks above the signal trace. The calculated onsets of the P- and S-wave at the various channels (ticks below the signal traces) could be used to assess the quality of location. In this figure the angle of incidence, the peak amplitude, and the source-receiver distance are given at the end of each signal.

In order to remove systematic location errors associated with picking errors and inaccuracy of assumed velocity we applied the joint-hypocenter determination (JHD) method (Douglas, 1967, Frohlich, 1979). In this method, we can determine "station corrections" that account for the inaccuracies of the wave velocity along the travel path especially near sensor positions. The source locations are iteratively calculated involving corrections of onset times. These corrections are estimated as the mean residual at each channel before each iteration. The iteration process is finished when corrections are becoming small enough.

5 MOMENT TENSOR EVALUATION

5.1 Pre-processing and extraction of data

We applied the moment tensor method to a selection of 15,526 events which were located using at least fifteen P- and S- wave arrival times. Signals striking the sensors from behind were ignored in the evaluation. In this case the sensor radiation pattern is poorly known. Since our goal is to estimate source mechanisms of many events in an automatic procedure, we have made a further selection in such a way that only events with a good signal-to-noise ratio were considered.

Input data for the moment tensor calculations are peak amplitudes and polarities of the first motion of the P-wave signal. We developed an automatic procedure for data extraction because inspection by eye is too time consuming for such a huge number of events. The data extraction procedure involves the following steps:

- Division of the signal amplitudes by the calibration factor of 335.1 V/(m/s) (the physical quantity measured by the sensors is supposed to be velocity).
- Conversion of velocity signals into displacement signals by integrating the data in the time domain.
- Band-pass filtering in the frequency range between 10 kHz and 500 kHz to remove high-frequency noise and signal offsets which eventually occurs due to integration.
- Cutting out traces using a defined time window of ±7.5 µs (151 samples) around the theoretical P-wave onsets.
- Only traces with a signal-to-noise ratio greater than 10 were considered for data extraction.
- Determination of first crossing of a threshold level of 10 per cent of the interval between peak amplitude within the 7.5 µs time window and noise level before signal onset at the rectified signal trace.
- Determination of the P-wave first motion which is the first minimum or maximum amplitude after the trigger point.

Figure 3 shows windowed time traces aligned at the times of first motion of the P-wave (ticks below the signal traces). It can be seen that the polarities of the P-wave first motion are in this case compressional at all channels. The following steps outline the treatment of data before moment tensor inversion calculations:

- Data were corrected for the measured sensor directivity.

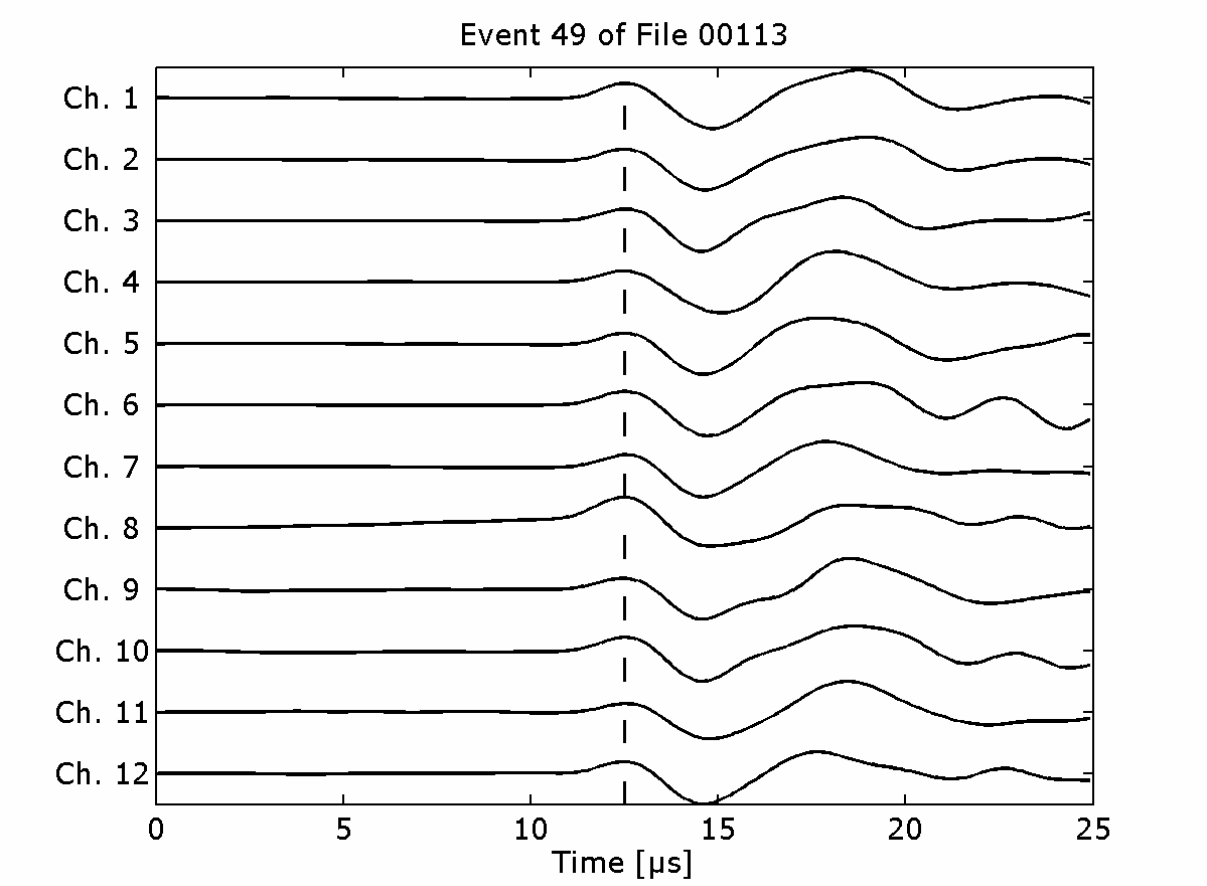

Figure 3: *Aligned P waveforms in a time window of 25 µs around the automatically picked first motion amplitude of the P-wave (marked by ticks above the signal traces).*

- Considering geometrical wave attenuation and damping (approximately -0.435 dB per 100 mm).
- Transformation of the source location coordinates and the normal vector components of the sensors into the north-east-down coordinate system.
- Calculation of the coefficient matrix a_{nk} from Equation (3).

After the data treatment the over-determined equation system (3) was solved for the six moment tensor components using singular-value decomposition (SVD).

5.2 Case study of moment tensor evaluation

In the following, the inversion method will be exemplarily applied to a data set of one event whose signals are displayed in Figure 2. The source mechanism is displayed by plotting the orientation of the principal axes which are obtained from the eigenvalues of the moment tensor (see **Figure 4**). The eigenvector of the largest eigenvalue gives the T (or tensional) axis direction; the eigenvector of the smallest eigenvalue gives the P (or compressional) axis direction, while the eigenvector associated with the intermediate eigenvalue gives the direction of the B (or null) axis. Note, that the P and T axes which are obtained from the motion on the fault plane, only coincide with the axes of maximum stress if the motion takes place on a newly formed fault plane. This is not the case if the motion takes place on a pre-existing plane of weakness. In principal, it is not possible to distinguish between motion on new planes or motion on pre-existing fault planes of weakness from the seismic radiation. Additional knowledge such as from stress measurements is necessary. Under consideration of this kind of

knowledge, it is assumed that P and T axes which were found from seismic radiation are somewhat indicative of the direction of stress.

The inversion method as presented in this work may lead to biased estimates if, for instance, the applied Green's functions are not appropriate to describe the wave propagation in the material, or the input data are inexact, or there is a large variability in sensor coupling, or if the source locations are not accurate enough. These uncertainties may lead to stability problems of the inversion calculations. Other stability problems may occur due to the small number of stations. An advantage of the sensor arrangement as presented in Figure 2 is good coverage of the focal sphere in all directions which is essential for the use of P-wave first motion data.

However, all mentioned uncertainties lead to errors in the estimated source mechanisms. Therefore we applied a so-called Jackknife test (Efron et al., 1986). The Jackknife test is a suitable test to check the influence of a single sensor onto the solution of the inversion calculations and to estimate their stability. As a means to visualize and quantify the scatter of principal axes orientations a bootstrap analysis (Efron et al., 1986) was used. For each event 250 moment tensor sets were generated by adding random errors to the moment tensor components within a confidence level of 99 per cent, i.e. within 2.35 standard deviations obtained from the Jackknife test. The eigenvectors of all 250 moment tensors were calculated and their directions P, B, and T were plotted as small dots in an equal-area projection onto the lower

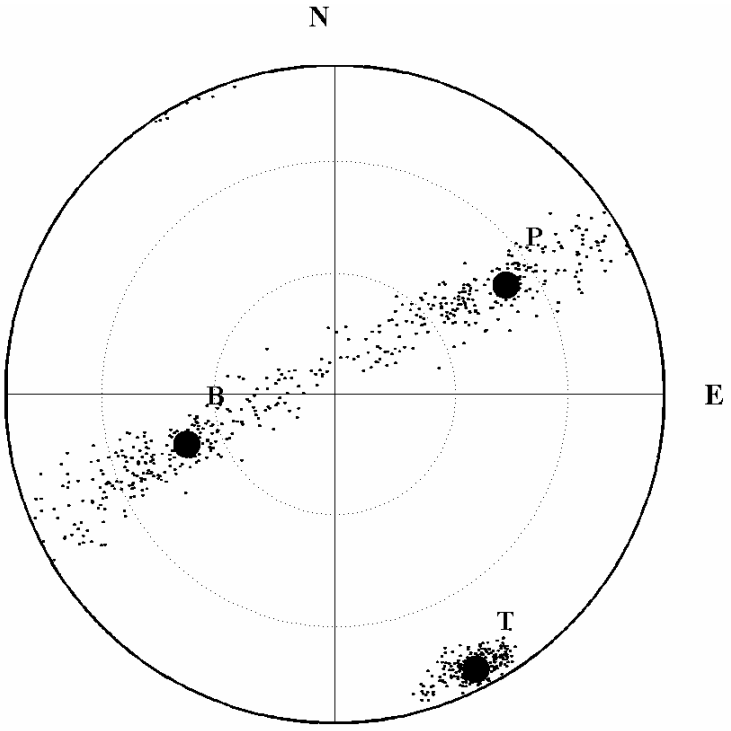

Figure 4: *Position of the mean T, B, and P axes (big dots) and their confidence areas (marked by small dots) which were estimated by the Jackknife test and bootstrap analysis.*

hemisphere. Figure 4 shows such a plot for the event of Figure 2. The big dots in this figure represent the average direction of the principal axes. The two dotted concentric circles indicate plunge angles (measured from horizontal direction downwards) of 30° and 60°. The figure shows that the T axis is nearly horizontal and its confidence area is fairly concentrated, whereas the overlapping confidence areas of the P and B axes form a broad strip which extends over the whole focal sphere in perpendicular direction to the T axis. The width of the confidence area is a measure of the stability of the solution. In the shown case, their width was not acceptable. Therefore, we looked for a more stable solution by trials where each time

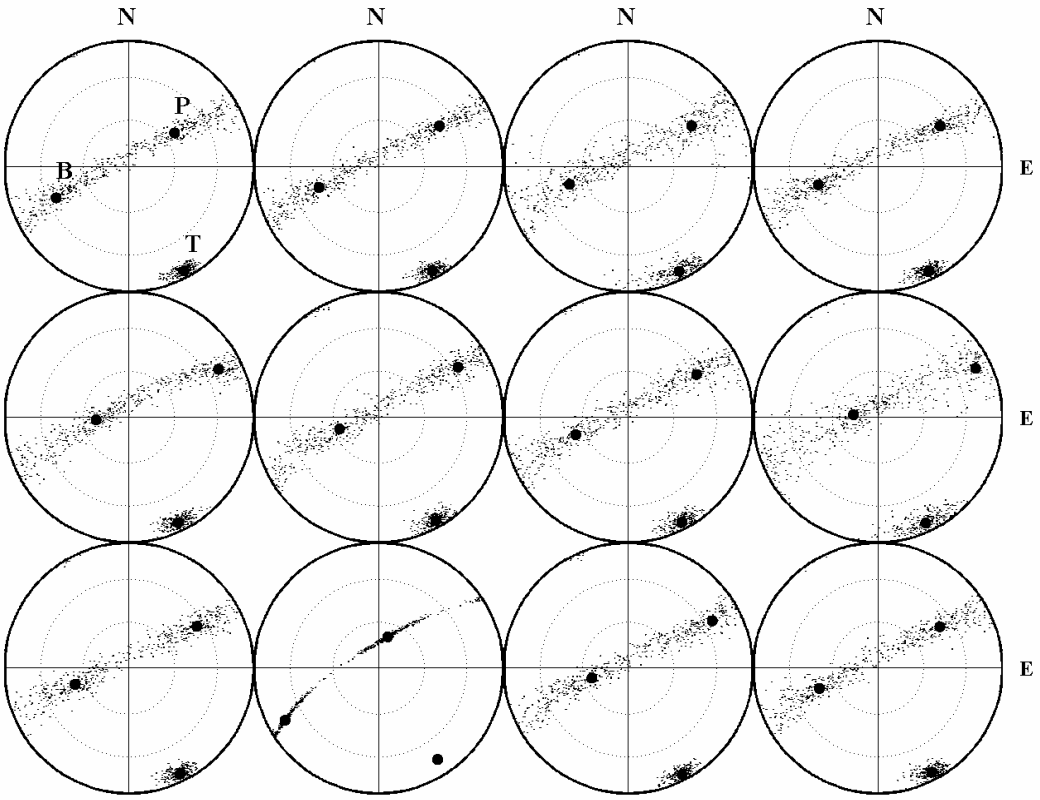

Figure 5: *Positions of the mean T, B, and P axes (big dots) and their confidence areas (small dots) which were estimated by the Jackknife test and bootstrap analysis with excluded channels 1 to 4 (plots at the first row), with excluded channels 5 to 8 (plots in the second row), and with excluded channels 9 to 12 (plots in the third row).*

the amplitude of one channel was removed from the input data set. The above mentioned procedure (Jackknife test plus bootstrap analysis) was repeated for each new data set obtained in such a manner.

The results of these tests are shown in **Figure 5** for the event from Figure 2. The plots in the upper row display calculations without channels 1 to 4 (from left to right), the plots in the second row display calculations without channels 5 to 8, and the plots in the third row display calculations without channels 9 to 12. The solution with the smallest width of the confidence area is obviously that without channel 10 (second plot in the third row), which consequently was excluded from the input data set in order to get stable solutions.

In order to quantify acceptable principal axes scattering we derived stability criteria on a set of 50 randomly selected events. Events were considered to be stable if the standard deviation of at least one of the three principal axes was less than 4°. Additionally the deviation between the observed and calculated first motion amplitudes must be less than 12 per cent. lf these conditions were not true the event was rejected and not considered for interpretation.

5.3 Influence of source type on extension of principal axes orientations

In some cases the confidence area is primarily enlarged in a specific direction depending on the source mechanism. There is obviously a direct relation between the extension of the confidence areas of the principal axes and the absolute values of the corresponding eigenvalues. For a pure double couple with two eigenvalues of equal absolute values the confidence areas of the T and P axes are similar. In the case of a pure tensile mechanism which has two equal eigenvalues having the same sign and a third eigenvalue of same sign but approximately

three time as large, only the confidence area of principal axis which corresponds to the dominant eigenvalue (T axes) is fixed. For a purely isotropic source, the three eigenvalues are equal; the position of the principal axes are not determined and, therefore, their confidence areas extend over the whole focal sphere.

Under the assumption that we have found events with stable inversion solutions through limitation of the confidence areas of the principal axes we can easily classify source mechanisms through the parameter $\varepsilon = e_2/max(|e_1|,|e_3|)$ where e_i are the eigenvalues of the moment

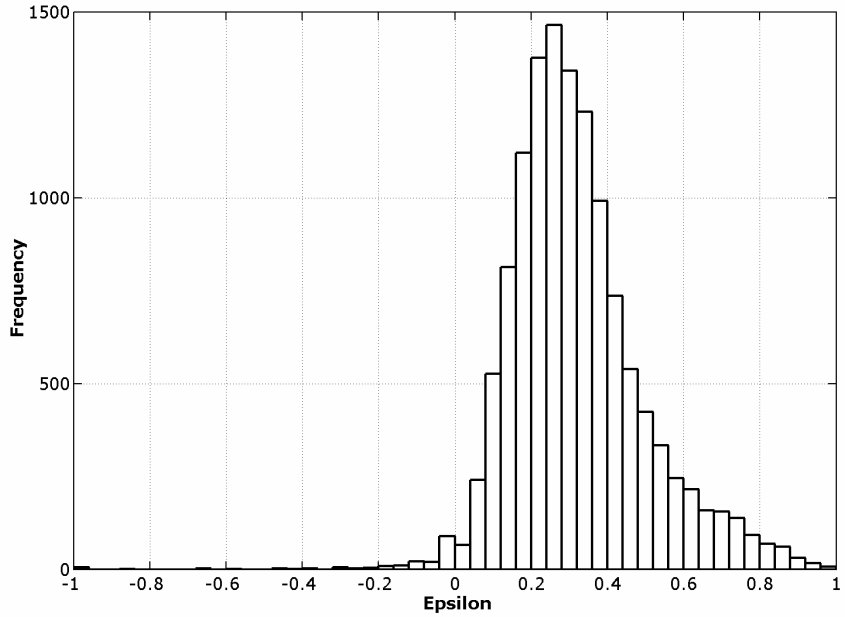

Figure 6: *Histogram of the ε values calculated by the eigenvalue of the moment tensor.*

tensor $(e_1 \geq e_2 \geq e_3)$. ε is zero for a shear mechanism, approximately 0.37 for a tensile mechanism for elastic parameters of rock salt, ±l.0 for an explosion and implosion mechanism, respectively, and 0.5 for a compensated linear vector dipole (Knopoff et al. 1970). **Figure 6** shows the histogram of ε values of 12,562 events which fulfilled the required stability criteria. The distribution is shifted to positive values with maximum at $\varepsilon = 0.32$ with tendency to values of a pure tensile mechanism ($\varepsilon = 0.37$).

5.4 Decomposition of the moment tensor

According to the results of the eigenvalue analysis, the focus of the evaluation of source mechanisms is on volume change in the sources and orientation of the fracture planes. For this purpose we choose a general decomposition of the moment tensor which is defined as:

$$M = \frac{1}{3} \cdot \begin{pmatrix} tr(M) & 0 & 0 \\ 0 & tr(M) & 0 \\ 0 & 0 & tr(M) \end{pmatrix} + \sum_{i=1}^{3} m_i^* \qquad (6)$$

where $tr(M) = m_1 + m_2 + m_3$ is the trace of the entire moment tensor and $m_i^* = m_i - 1/3 \cdot tr(M)$ are deviatoric eigenvalues. The first term describes the isotropic part of the moment tensor which is important for quantifying the volume change in the source. The second term describes the deviatoric part of the moment tensor. The deviatoric part can be further decomposed. Various decompositions are possible. In the field of AE we choose a frequently used decomposition into double couple (DC) and compensated linear vector dipole (CLVD). Of

course, the DC mechanism is a realistic one for microcracks. The CLVD mechanism raises the question: is this mechanism realistic for microcracks or not? In seismology, significant CLVD mechanisms can be found for deeper earthquakes or earthquakes with two or more subevents at a complicate fractal geometry of the fault plane (Frohlich, 1994, Miller et al., 1998).

The combination of isotropic and CLVD components describes a tensile source. A pure tensile source can be represented by setting the isotropic part as 79.6 per cent (for elastic constants of rock salt) and the CLVD part as 100 per cent. In a broader sense, CLVD source components can be interpreted as the deviatoric part of a tensile source in case of microcracks.

In addition to the above mentioned decomposition, the source mechanisms can be quantified using the R value which is defined after Feignier et al. (1992) as the ratio of isotropic component and sum of isotropic and deviatoric component:

$$R = \frac{tr(M)}{|tr(M)| + \sum_{i=1}^{3} |m_i^*|} \qquad (7)$$

The ratio varies from –100 per cent for pure implosion sources up to 100 per cent for pure explosion sources. A pure shear failure mechanism is indicated by R = 0 and a pure tensile mechanism is indicated by a R value of approximately 67 per cent for the elastic parameters of rock salt.

The volume change in the source can be estimated from the isotropic moment tensor $M_{ISO} = (\lambda + 2/3\mu)\Delta V$ (λ, μ are the Lamés constants) which is applicable to plane cracks with tensile source components (Müller, 2001). According this relationship the crack volume can be estimated from the scalar moment M_{ISO} of the isotropic moment tensor as: $\Delta V = M_{ISO}/(\lambda + 2/3\mu)$. After Silver and Jordan (1982) the scalar moment M is defined as:

$$M = \frac{\left|\sum_{j=1}^{3} e_j\right|}{\sqrt{6}},$$

where e_j are the eigenvalues of the isotropic moment tensor. It should be noted that alternative definitions of the scalar moment were considered in literature (see Dziewonski et al. 1983, Silver et al., 1982, and Hudson et al. 1989). Bowers et al. (1999) compare various published definitions of scalar moments which were derived from the seismic moment tensor. They found differences between seismic moments suggested by Silver and Jordan (1982) and Hudson et al. (1989) by a factor that varies between 1.2 and 0.8 (for a Poisson solid).

6 RESULTS OF THE MOMENT TENSOR CALCULATIONS

6.1 Effectivity of automated evaluation procedures

Table 1 presents the number of events which were evaluated with various automatic procedures. The table shows, that 57 per cent of all 10^5 detected events were located using at least eight P- and S-wave arrivals times, 30 per cent of all events were more precisely located using 16 arrivals at least. The source mechanism could be evaluated using the moment tensor method on about 15 per cent of all events, and stable moment tensor solutions were obtained on 10 per cent of the events.

Table 1: Number of events which were obtained in automatic procedures such as registration of events up to moment tensor determination.

Procedure	**Requirements**	**Number of events**
Registration of events	at least one channel was hit	10^5 (100 per cent)
Source location	at least eight P- and S-wave consistent arrival times	$5.7 \cdot 10^4$ (57 per cent)
Precise source location	at least 16 P- and S-wave consistent arrival times	$3 \cdot 10^4$ (30 per cent)
Moment tensor method	at least 10 clear discernible P-wave first motions	$1.5 \cdot 10^4$ (15 per cent)
Stable moment tensor solutions	at least 10 clear discernible P-wave first motions	$1.25 \cdot 10^4$ (12.5 per cent)

6.2 Source mechanism and source orientation

As mentioned above, the moment tensor method was applied to 12,562 events which fulfilled the required stability criteria. The following analysis exclusively concentrates on these events. In a more detailed analysis the AE activity was divided in five successive stages of the test. At low axial stress up to 20.8 MPa the rock behaves nearly linear elastic. Above this axial stress the rock becomes dilatant. In the dilatancy region where most of the events were recorded, stages with equal number of events were selected. The four further stages are from 20.8 to 30.2 MPa, from 30.2 to 34.1 MPa, from 34.1 to 37.8 MPa, and from 37.8 to 44.1 Mpa, respectively. Please note that the highest axial stress of 44.1 MPa does not correspond to the stress at fracture. The ultimate axial stress is approximately 55 to 60 MPa. Above 44.1 MPa most of the AE sensor cables were ruptured due to the high deformation of the specimen and, therefore, the AE measurement has been stopped.

Figure 7 displays in its upper part the position of T axes in a vertical coordinate plane (x-z-plane) and in its lower part the density of T axes in an equal-area projection to the lower hemisphere in the above-mentioned five stages. The figure shows at top the T axes by means of small dashes which were rotated in such a way that the axes lie in the vertical coordinate planes. The z axis corresponds to the loading direction. The shape of the contour of the rock specimen at the end of each stage is plotted as a box. Apart from few events which were recorded at the beginning of the test (figure at the left-hand side) most of the T axes are nearly horizontal orientated. The T axes distribute around the focal sphere at plunge below 30°. One accumulation of events has been formed in direction of approximately 54° in azimuth (measured clockwise from top) and of 15° in plunge which becomes stronger with increasing axial stress.

In order to study the distribution of the isotropic and double-couple components the events were separated into two fractions: events with exclusively compressional first motions and events with dilatational first motion at least at one channel. The latter fraction includes only about 2.5 per cent of all events. The histograms of the isotropic and double-couple components of both fractions are shown in **Figure 8.** The distribution of the fraction with compressional first motion is indicated by unfilled bars, the other with partly dilatational first motion is indicated by filled bars. Apart from the events with pure deviatoric components which are indicated by the peak at zero per cent, the distribution of the isotropic part (Figure 8a) is very wide with its maximum at 50 per cent. Most events with dilatational first motion show lower isotropic components with its maximum near zero per cent.

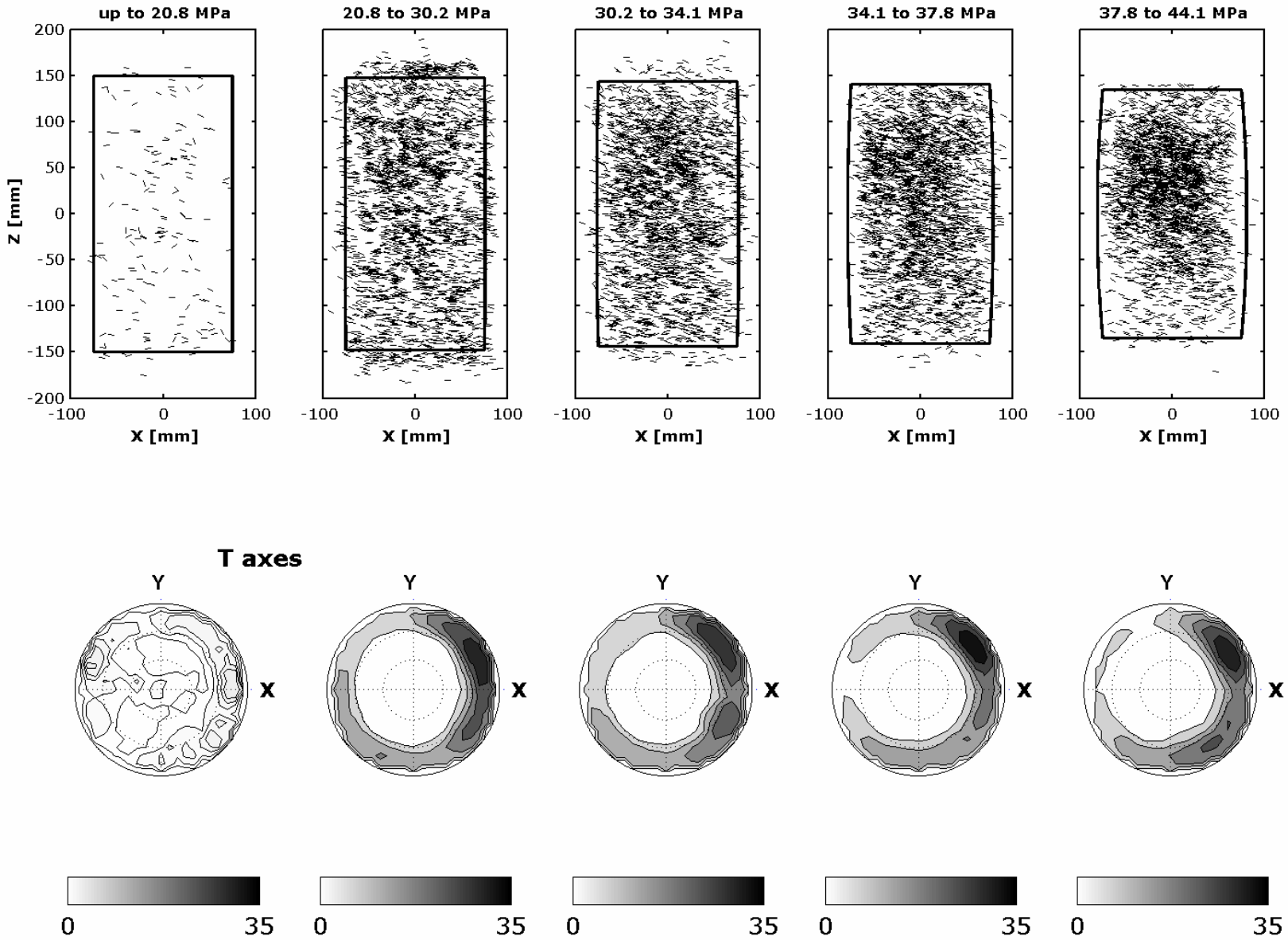

Figure 7: At top: position of T axes marked by small dashes which are lying in the vertical x-z-projection plane in five successive stages. The black boxes are the contour of the specimen after reaching the final stress at each stage. At bottom: distribution of the T axes in an equal-area projection on the lower hemisphere.

Figure 8b shows the distribution of the DC components. The frequency of events increases up to approximately 25 per cent and after a broad maximum slightly decreases. Events with partly dilatational first motion show a fairly flat distribution beginning at about 10 per cent.

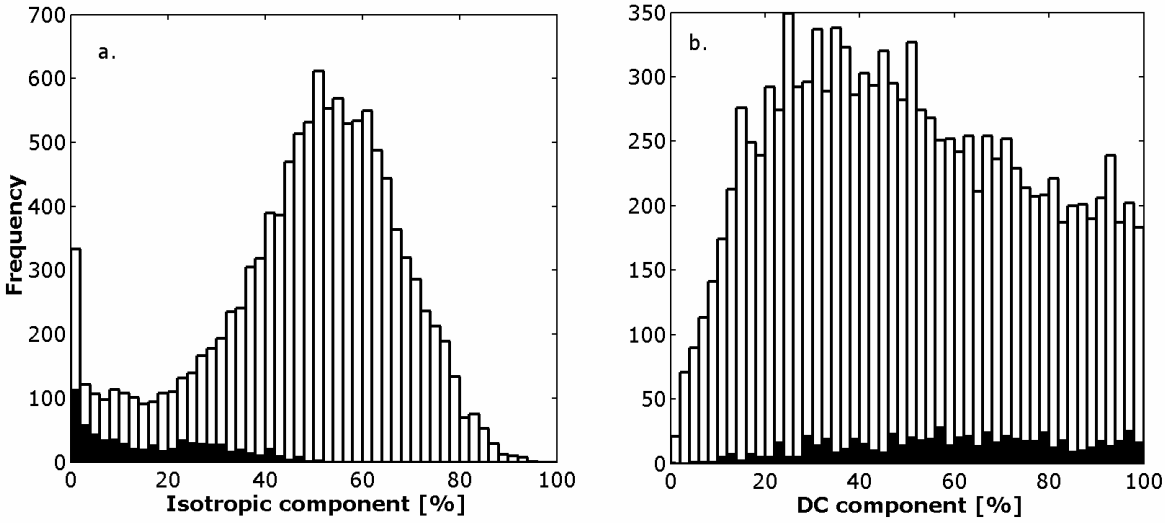

Figure 8: *Histogram of isotropic source component (a.) and double-couple component (b.) of all evaluated events. Unfilled bars are indicating events with compressional first motions only and black bars are indicating events with at least one dilatational first motion.*

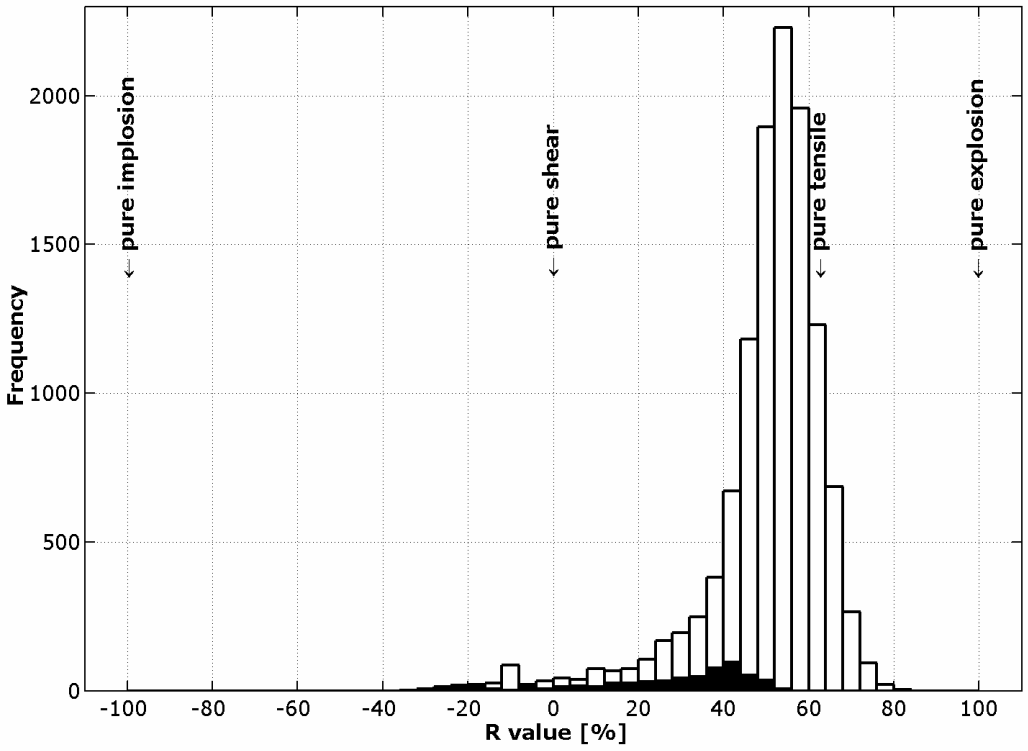

Figure 9: *Histogram of R value of all evaluated events. The R values of pure explosional sources , pure implosional sources, pure shear sources, and pure tensile sources are marked by arrows.*

Figure 9 shows the distribution of the R value of all evaluated events. Additionally, the specific R values of a pure implosional source at -100 per cent, pure explosional source at 100

per cent, pure shear source at R = 0 per cent, and pure tensile source at 67 per cent are marked by arrows. The R values show a peaked distribution with maximum at 54 per cent close to the R value of a pure tensile source. At higher values the distribution quickly tails off. At lower R values the tail reaches down to negative values indicating the presence of few events with partly implosional source components. It can be seen that the predominant source mechanism is of tensile type. Pure explosional sources do not occur.

The distribution of the volume change (**Figure 10**) shows that most of the events have volume changes below about 50 mm^3 with a pronounced increase to very small values. The total amount of dilatancy calculated from the moment tensors by adding up the volume

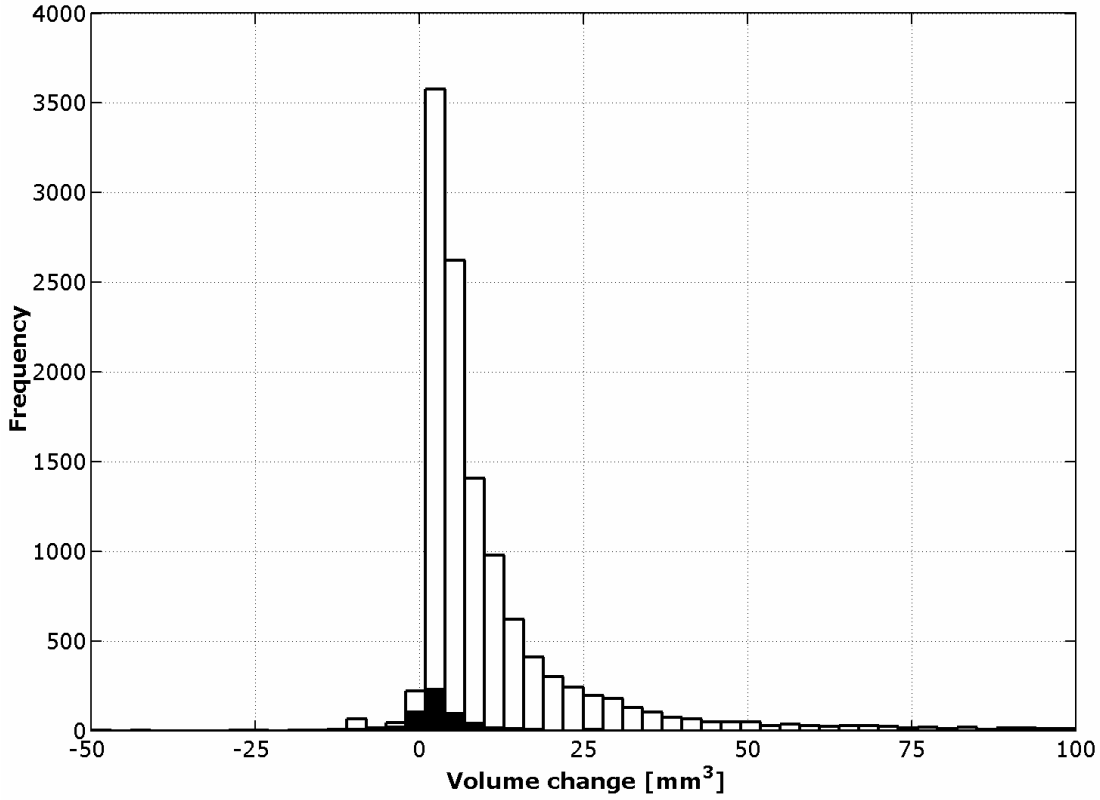

Figure 10: *Histogram of volume change (in mm^3)of the sources.*

change of all events is about 150 ml. The survey of the rock specimen after the test pointed out that the average diameter of the rock specimen had increased from originally 150 mm to 158.2 mm and that the final axial deformation was about 26.4 mm. According to these dimensions the actual dilatancy of the specimen was about 75.6 ml. That means, that the calculated dilatancy is two times higher than the measured one. It can be even more, because small events, which are not considered in the moment tensor evaluation, contribute to the volume, but with much smaller amount than the big events. This discrepancy between measured and calculated dilatancy can be explained by the fact that open cracks were partly closed due to the applied confining pressure. This suggests that some of the opened cracks close during further loading of the specimen.

As mentioned before the majority of evaluated events have compressional P-wave first motions at all channels which is a clear indication for tensile fracturing. The few events with partly dilatational first motion tend to higher DC components and lower isotropic components. The volume change in the source of these events is nearly zero. This is an indication that particular events with high shear components occurred. If such sources exist they could be generated by stress deviations at increasing axial load. Under deviatoric stress conditions planes of maximum shear stress are orientated at 45° from planes of maximum normal stress.

But planes of maximum shear stress are not generally free of normal stress. Additional information e.g. from S-wave first motions, could better explain the existence of DC components, because sources of dominant shear type radiate more energy in S waves than in P waves. Unfortunately, S-wave first motions are not clearly discernible in our recorded signals (cf. Figure 2) because of the small time separation between P- and S-wave arrivals and the presence of P waves reflected at the specimen walls which can arrive earlier or at the same time as direct S waves.

7 DISCUSSION

Two types of microcracks are observed in rock salt under dilatant loading. Cracks of Type 1 are inter-crystalline cracks which cause tensile opening at grain boundaries and cracks of Type 2 are intra-crystalline cracks or transcrystalline cracks on crystallographic planes (cleavage planes) within a grain (Alkan et al., 2002). The latter kind of cracks causes no opening of crack surfaces.

During loading, cracks of Type 1 are formed at grain boundaries which are favourably orientated in direction of the maximum principal stress, this is in our experiment in axial direction of the cylindrical specimen. With increasing load neighbouring cracks become more frequent and grow together to one jointed crack which may extend even over several neighbouring grains. The direction of opening is perpendicular to maximal compression. Consequently, crack Type 1 is responsible for dilatancy and an increase of permeability for fluids.

The here evaluated acoustic emission events are mainly caused by cracks of dilatant Type 1. There are several indications which confirm this fact. First, the source location discovers a cellular structure with a cell size in the range of some grain diameters. The events occurred in zones where cell interfaces are favourably orientated in the stress field. Second, most of the events (approximately 90 per cent) show significant isotropic source components which is in good agreement with dilatation of salt rock during compression. Their ε values and R values (Figure 22 and 25) which were obtained from eigenvalues of the moment tensors tend to values of pure tensile mechanisms ($\varepsilon = 0.37$ and $R = 67$ per cent). And third, we found that the tension (T) axes which are normal to the crack plane of tensile cracks were predominantly orientated in radial direction, that means normal to the direction of the maximum principal stress as expected for such kind of crack type.

ACKNOWLEDGEMENT

The author thanks his colleague Dr. J. Eisenblätter and Prof. T. Dahm from the University of Hamburg, Germany, for discussion and their suggestions and interests. The author would like to thank Dr. U. Düsterloh and Mr. R. Niens from the Technical University of Clausthal, Germany, for the performance of the experiment. We are grateful to Dr. T. Spies and Dr. J. Hesser (Federal Institute for Geosciences and Natural Resources, Hannover, Germany) for providing us with the AE measuring system.

REFERENCES

Aki, K., Richards, P. G., 2002: *Quantitative Seismology*, Second Edition, University Science Books, Sausalito, California.

Alkan, H., Pusch, G., 2002: *Definition of the Dilatancy Boundary Based on Hydro-Mechanical Experiments and Acoustic Detection,* SMRI Fall Meeting, Bad Ischl, Austria, Oct. 7-9, 2002.

Bowers, D., Hudson, J., A., 1999: *Defining the Scalar Moment of a Seismic Source with a Gerneral Moment Tensor,* Bull. Seis. Sc. Am., Vol. 89, No. 5, pp. 1390-1394.

Brace, W. F., Paulding, B., W., Scholz, C., 1966: *Dilatancy in the fracture of crystalline rocks,* J. Geophys. Res., Vol. 71 (16), pp. 3939-3953.

Douglas, A., 1967: *Joint hypocenter determination*, Nature, 215, pp. 47-48.

Dziewonski, A. M., Woodhouse, J., H., 1983: *An experiment in systematic study of global seismicity: centroid-moment solution for 201 moderate and large earthquakes,* J. Geophys. Res., Vol. 88, pp. 3247-3271.

Efron, B., Tibshirani, R., 1986: *Bootstrap methods for standard errors, confidence intervals and other measures of statistical accuracy*, Statistical Science, Vol. 1, pp. 54-77.

Eisenblätter, J., 1980: *The origin of acoustic emission – Mechanisms and models,* in: Acoustic Emission, Conference in Bad Nauheim, Deutsche Gesellschaft für Metallkunde e.V., pp. 189-204.

Feignier, B., Young, R. P., 1992: *Moment Tensor Inversion of Induced Microseismic Events: Evidence of Non-Shear Failure in the -4<M<-2 Moment Magnitude Range*, Geophys. Res. Letters, Vol. 19, No. 14, pp. 1503-1506.

Frohlich, C., 1979: *An Efficient Method for Joint Hypocenter Determination for Large Groups of Earthquakes.* Computers and Geosciences, Vol. 5, pp. 387-389.

Frohlich, C., 1994: *Earthquakes with non-double-couple mechanisms.* Science, Vol. 264, pp. 804-809.

Gilbert, F., 1970: *Excitation of the normal modes of the earth by earthquake sources.* Geophys. J. R. Astr. Soc. Vol. 22, pp. 223-226.

Hudson, J., A., Pearce, R., G., Rogers, R., M., 1989: *Source plot for inversion of moment tensors,* J. Geophys. Res., Vol. 94, pp. 765-774.

Hunsche, U., Hampel, A., 1999: *Rock Salt – the mechanical properties of the host rock material for a radioactive waste repository,* Engineering Geology, Vol. 52, pp. 271-291.

Jost, M. L., Herrmann, R. B., 1989: *A student's guide to a review of moment tensors*, Seis. Res. Letters, Vol. 60, pp. 37-57.

Lockner, D., Byerlee, J., 1977: *Hydrofracture in Weber Sandstone at high confining pressure and differential stress*, J. Geophys. Res., Vol. 82, pp. 2018-2026.

Lux, K-H., Düsterloh, U., Hou, Z., 2000: Increasing the Profitability of Storage Caverns by Means of a New Dimensioning Concept (I), Erdöl Erdgas Kohle, Vol. 118, pp. 294-300.

Manthei, G., Eisenblätter, J., Spies, T., 2000: *Acoustic Emission in Rock Mechanics Studies,* in: Acoustic Emission – Beyond the Millennium, Eds.: Kishi, T., Ohtsu, M., Yuyama, S., Elsevier, pp. 127-144.

Miller, A. D., Foulger, G., R., Julian, B. R., 1998: *Non-double-couple earthquakes. 2. Observations,* Rev. Geophys., Vol. 36, pp. 551-568.

Pujol, J., Herrmann, R., B., 1990: *A student's guide to point sources in homogeneous media,* Seis. Res. Lett., Vol. 61, No. 3-4, pp. 209-224.

Scholz, C., H., 1968a: *Microfracturing and the Inelastic Deformation of Rock in Compression,* J. Geophys. Res., Vol. 73, No. 4, pp. 1417-1432.

Silver, P. G., Jordan, T. H., 1982: *Optimal estimation of scalar seismic moment,* Geophys. J. R. Astr. Soc., Vol. 70, pp. 755-787.